Review

Optical coupling of individual air-suspended carbon nanotubes to silicon microcavities

By Wataru TERASHIMA[*1] and Yuichiro K. KATO[*1 *2,†]

(Edited by Maki KAWAI, M.J.A.)

Abstract: Carbon nanotubes are a telecom band emitter compatible with silicon photonics, and when coupled to microcavities, they present opportunities for exploiting quantum electrodynamical effects. Microdisk resonators demonstrate the feasibility of integration into the silicon platform. Efficient coupling is achieved using photonic crystal air-mode nanobeam cavities. The molecular screening effect on nanotube emission allows for spectral tuning of the coupling. The Purcell effect of the coupled cavity-exciton system reveals near-unity radiative quantum efficiencies of the excitons in carbon nanotubes.

Keywords: carbon nanotubes, silicon photonics, microcavity, cavity quantum electrodynamics, Purcell effect

1. Introduction

Advances in silicon photonics have been expanding the capabilities of monolithic photonic circuits,[1),2)] and the integration of semiconducting nanomaterials would allow for further scaling and increased functionality. In this regard, carbon nanotubes (CNTs) are promising because they can be directly synthesized on silicon,[3)] and they are telecom band emitters[4),5)] that do not exhibit absorption loss by silicon. Electrically gated *pn*-junction devices can also be constructed, where extremely efficient photocurrent generation[6)–8)] and excitonic electroluminescence[9),10)] have been demonstrated. Furthermore, unique exciton physics gives rise to telecom band single-photon emission at room temperature.[11)–14)] In particular, using as-grown air-suspended CNTs is attractive because they are free of defects[15),16)] and they provide high luminescence yields.[17)]

Coupling to photonic structures is essential to utilize such characteristics in monolithic optical circuits. In particular, microcavities offer quantum electrodynamical effects for increased performance and functionality by confining electric fields into a small mode volume. Exciton polaritons can form when nanotube emission is strongly coupled to a cavity,[18)] whereas interaction of CNTs with cavities results in an increased spontaneous emission rate in the weak coupling regime.[19)–23)]

Here, we review our efforts on coupling as-grown individual air-suspended CNTs to optical microcavities and discuss cavity quantum electrodynamical effects in such systems. In Section 2, we introduce microdisk resonators to demonstrate coupling with air-suspended CNTs.[24)] More efficient coupling is achieved in specially designed air-mode nanobeam cavities,[25)] as described in Section 3, and a method for spectrally tuning the coupling[26)] is discussed in Section 4. Finally, in Section 5, the Purcell effect in single CNTs is studied to show that the radiative quantum efficiency of bright excitons can reach near unity at room temperature.[27)]

2. Optical coupling to silicon microdisk resonators

Microdisk resonators are a commonly used microcavity structure, supporting whispering gallery modes (WGMs) where optical waves are guided along the circumference of the disk by continuous internal reflection. Because they can have ultra-

[*1] Nanoscale Quantum Photonics Laboratory, RIKEN Cluster for Pioneering Research, Wako, Saitama, Japan.
[*2] Quantum Optoelectronics Research Team, RIKEN Center for Advanced Photonics, Wako, Saitama, Japan.
[†] Correspondence should be addressed to: Y. K. Kato, Nanoscale Quantum Photonics Laboratory, RIKEN Cluster for Pioneering Research, 2-1 Hirosawa, Wako, Saitama 351-0198, Japan (e-mail: yuichiro.kato@riken.jp).

doi: 10.2183/pjab.100.022

high quality factors[28),29)] and small mode volumes, WGMs are suited for coupling with nanoscale emitters such as quantum dots.[30)–32)] It is relatively easy to tune the cavity resonance to the emitter wavelength by fabricating disks with an appropriate diameter, and the three-dimensional structure of post-supported microdisks[30),31),33)] is compatible with air-suspended CNTs. Furthermore, they can be coupled to waveguides with high efficiency because they are traveling-wave resonators,[29)] making them a preferred choice compared with planar cavities[34)–37)] for integration in silicon photonics.

In this section, we describe the integration of individual CNT emitters with silicon microdisks using fabrication processes compatible with standard silicon photonics.[24)] When photons emitted from nanotubes are coupled to the WGMs of the microdisks, emission enhancement occurs in narrow spectral windows corresponding to the modes. Spatial imaging of the emission at the WGM wavelength shows the disk periphery illuminated by the coupled CNT emission that circulates within the microdisk.

The microdisks are fabricated from a silicon-on-insulator wafer with a 260-nm-thick top Si layer and a 2000-nm-thick buried oxide layer. Electron beam lithography and dry-etching processes form doughnut-shaped trenches in the top Si layer. The buried oxide layer is etched in buffered hydrofluoric acid to create a post-supported disk structure. A scanning electron microscope image of a typical microdisk before nanotube growth is shown in Fig. 1(a).

To integrate CNT emitters with silicon microdisks, another electron beam lithography step is performed to define catalyst windows at the outer edges of the doughnut-shaped trenches. Single-walled CNTs are grown by chemical vapor deposition using ethanol as a carbon source.[38)] The catalyst solution is prepared by ultrasonicating 5.0 mg of cobalt(II) acetate tetrahydrate and 50.0 mg of fumed silica in 40.0 g of ethanol. We spin coat and lift off the catalyst solution, and the samples are annealed in the air for 5 min at 400°C before growth. The samples are then placed in a quartz tube furnace, and the temperature is elevated to 800°C while flowing Ar with 3% H_2. Ethanol is introduced by bubbling the carrier gas for 10 min. With some probability, nanotubes can become suspended across the trench onto the microdisk [Fig. 1(b)]. By controlling the size of the catalyst areas, we can obtain a reasonable yield of ∼10% for microdisks with single suspended tubes. We note that the yield can be easily increased by placing more catalysts if devices with multiple nanotubes are acceptable.

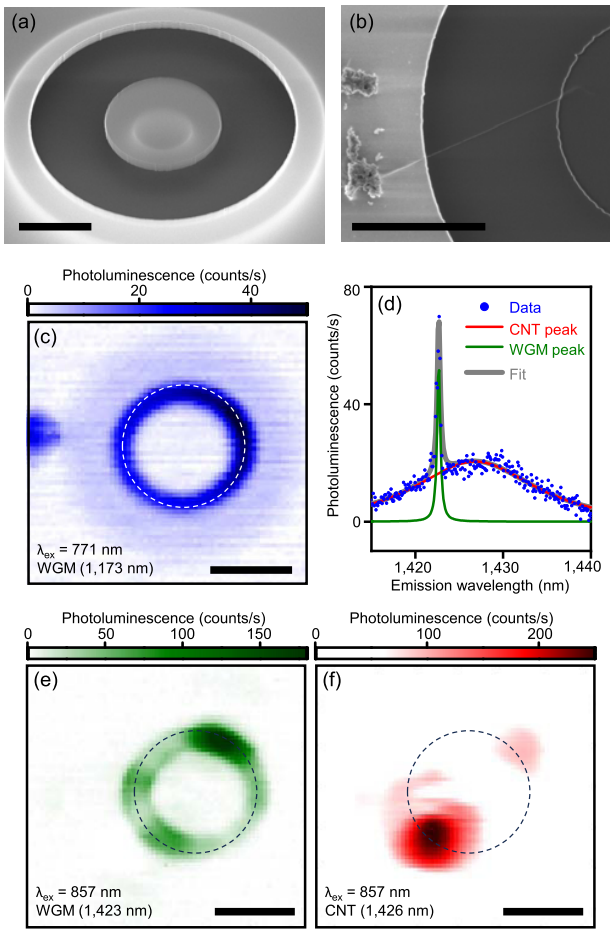

Fig. 1. (Color online) (a) Scanning electron micrograph of an as-fabricated Si microdisk. (b) Scanning electron micrograph of a suspended nanotube attached to a microdisk. (c) A photoluminescence (PL) image of Si emission coupled to a whispering gallery mode (WGM), taken with $\lambda_{ex} = 771$ nm and $P = 1.5$ mW. The spectra have been integrated from 1171 to 1175 nm to construct this image. (d) High-resolution PL spectrum of nanotube emission coupled to a WGM. Dots are data, and lines are Lorentzian fits. The peak values obtained from the fits are plotted in (e) and (f). (e) A PL intensity mapping for carbon nanotube (CNT) emission coupled to a WGM. (f) A PL intensity mapping for direct CNT emission, taken with $\lambda_{ex} = 857$ nm and $P = 0.3$ mW with circular polarization. The scale bars in the images are 2 μm. The dotted circles in (c), (e), and (f) represent the Si microdisk. Original data are presented in Ref. 24.

The devices are characterized by a home-built laser-scanning confocal photoluminescence (PL) microscopy system.[19),39),40)] An output of a continuous-wave Ti:sapphire laser with a power P

and a wavelength λ_{ex} is focused onto the sample using an objective lens to a spot size of $\sim$1 μm. PL is coupled to a 300-mm spectrometer through a pinhole in a confocal configuration. An InGaAs photodiode array is used for detection, and PL images are collected with a steering mirror.

The photons that couple to the WGM circulate within the microdisk, which can be visualized via spectrally resolved PL imaging. In the case of WGM at Si emission wavelengths [Fig. 1(c)], PL is enhanced at the edges of the disk. Using a higher-resolution grating, we collect PL spectra as we raster the laser spot over the scan area and fit them with a bi-Lorentzian function corresponding to the WGM and direct CNT emission peaks [Fig. 1(d)]. We determined that the measured quality factor of the WGM is limited to $\sim$3000 because of spectrometer resolution, which is already two orders of magnitude larger compared with a simple planar cavity.[34)]

Spectrally resolved PL images corresponding to the WGM and direct CNT emission are presented in Fig. 1(e) and (f). Nanotube emission coupled to the WGM circulates within the disk and illuminates the circumference [Fig. 1(e)], showing that CNT emission is efficiently guided into the silicon photonic structure. We note that the coupling occurs through the evanescent fields of the WGM, as the nanotube is located outside the resonator. This contrasts with the case of quantum dots embedded within the microdisks, and our results show that the evanescent fields are strong enough to couple the nanotube emission into the WGM.

The direct emission from the CNT is centered on the nanotube itself as expected [Fig. 1(f)], although one can observe a lower-intensity spot at the opposite side of the disk. We interpret the existence of such a remote spot in terms of the in-plane Fabry-Perot mode within the microdisk.[32)] Such an interpretation is also consistent with the image of the WGM [Fig. 1(e)], which shows larger intensity near that spot.

3. Air-mode photonic crystal nanobeam cavities for high-efficiency coupling

A fundamental issue exists in efficiently coupling air-suspended nanotubes to silicon microcavities. The fields of the cavity modes are typically confined within silicon, which is the high-index material, and optical coupling relies on relatively weak evanescent fields. Mode profiles must be engineered to increase the field intensities in air to make use of the PL from air-suspended nanotubes. In this aspect, photonic crystal nanobeam cavities offer flexible control over the cavity fields, and better coupling than microdisk resonators is expected because nanocavities with smaller mode volumes can be designed.

In a nanobeam cavity, a periodic array of air holes is etched into a waveguide to form a photonic bandgap, which acts as a Bragg reflector. The bands below the gap are called dielectric bands because the field amplitudes are maximized within the dielectric material. The bands above the gap are known as air bands because they have large fields in the air holes. The dielectric band modes can be confined by locally reducing the lattice constant a, as the energy of the modes will become higher and the photons will be surrounded by the photonic band gap.[41),42)] Similarly, air band modes can be confined by introducing a larger lattice constant region.[43),44)]

This section demonstrates high-efficiency spontaneous emission coupling for a single CNT coupled to a silicon photonic crystal nanobeam cavity with an ultralow mode volume.[25)] We take advantage of the excellent optical properties of as-grown air-suspended CNTs[7),39),45),46)] and integrate them with specially designed cavities with large fields in the air, distinctly different from the standard dielectric-mode cavities.[42),47)–50)]

We fabricate the photonic crystal nanobeam cavities from 260-nm-thick silicon-on-insulator similar to microdisks as described in Section 2. Electron beam lithography and dry etching processes form the nanobeam structure with a width of 670 nm, and the buried oxide layer is removed by wet etching. The cavities are designed to have reduced or increased lattice constant in a parabolic manner[41),42),48)] over 12 periods for dielectric- and air-mode cavities, respectively. The lattice constants and hole sizes have been selected to match the nanotube emission wavelengths. The emission properties of devices are characterized using a home-built confocal microspectroscopy system.[19),39),40)] The laser polarization angle is adjusted to maximize the PL signal unless otherwise noted.

Electron microscope images of typical devices are shown in Fig. 2(a) and (b). We have performed finite-difference time-domain (FDTD) calculations for these cavity structures to map out the profiles of the fundamental modes. Because nanotubes will be lying at the top surface of the nanobeam, we plot the mode profiles at that height in Fig. 2(c) and (d). As expected, the dielectric-mode cavity has high field amplitudes within the Si material,

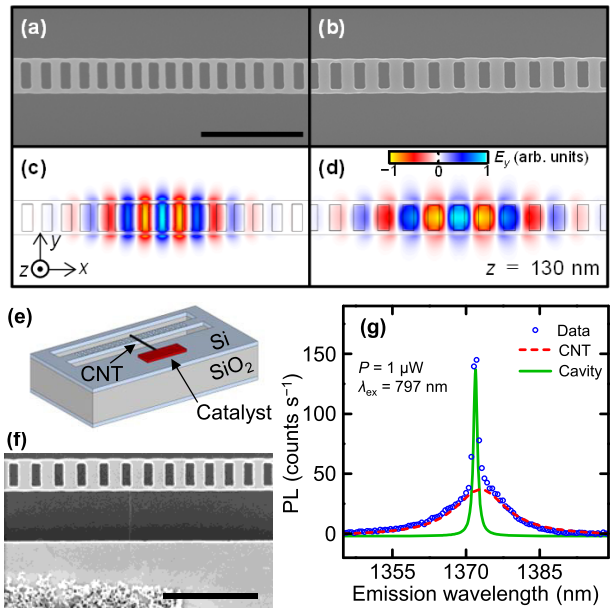

Fig. 2. (a, b) Scanning electron micrographs of (a) dielectric- and (b) air-mode photonic crystal nanobeam cavities, respectively. (c, d) Profiles of normalized y-component of electric fields E_y at $z = 130$ nm. The origin of the coordinate system is the center of the cavity. For (c), a dielectric-mode cavity with $a = 390$ nm, cavity-center period of $0.84a$, and 200 nm by 530 nm holes is used for the calculation. For (d), an air-mode cavity with $a = 430$ nm, cavity-center period of $1.16a$, and 220 nm by 510 nm holes is used. Panels (a–d) share the 2 μm scale bar in (a). (e) A schematic of a device with an individual carbon nanotube (CNT). (f) Scanning electron micrograph of a device with a suspended nanotube. The scale bar is 2 μm. (g) Typical photoluminescence (PL) spectrum of an air-mode device coupled to a nanotube. The dots are data, and the lines are Lorentzian fits. Original data are presented in Ref. 25.

with evanescent fields extending out the edges. For the air-mode cavity, the fields are mostly distributed within the air holes, and there are some evanescent fields as in the case of the dielectric-mode cavity. The intense fields in the air holes should be an advantage compared with cavities that confine most of the optical fields in the high-index medium[19),24),51)] because nanotube PL is quenched when they are in contact with the substrate.[39),52)] We note that both cavity modes are transverse electric modes. Therefore, polarization matches with nanotube emission perpendicular to the nanobeams.

To couple individual CNTs to nanobeam cavities, we have fabricated devices shown as a schematic in Fig. 2(e). Catalyst particles are placed across a trench from the cavity, and we perform chemical vapor deposition to grow CNTs onto the cavities as described in Section 2. An electron micrograph of a device after nanotube growth is shown in Fig. 2(f).

We present a PL spectrum from one of such devices taken with $P = 1$ μW and $\lambda_{ex} = 797$ nm in Fig. 2(g). On top of the broad direct emission from the nanotube, there is a very sharp peak, the cavity mode, indicating that the nanotube emission is optically coupled to the cavity.

The emission enhancement at the cavity resonance occurs because of a quantum electrodynamical phenomenon known as the Purcell effect[53)] that alters the decay dynamics of emitters in microcavities. In free space, the total decay rate can be written as $\gamma_r + \gamma_{nr}$ where γ_r and γ_{nr} are the radiative and nonradiative decay rates, respectively. When the emitter is coupled to a microcavity, the increased photon density of states gives rise to an additional radiative decay rate $F\gamma_r$, where F is the Purcell factor.[14),21)–23),25),26)] The accelerated radiative recombination appears in the spectral domain as an increased intensity in a spectrally narrow region corresponding to the cavity mode.

We have performed confocal PL imaging on those devices coupled with single CNTs to locate the nanotube positions. By determining the positions of the highest PL intensity from images of > 30 devices, the spatial displacements of the nanotubes with respect to the center of the cavities have been mapped out [Fig. 3(a) and (b)]. It is possible to identify qualitative differences in the spatial distribution of nanotubes between the two types of cavities. The emission spot of nanotubes is mainly located at the edges of the nanobeam or within the trench for the dielectric-mode cavities. The emission is on top of the nanobeam itself for the air-mode cavities.

These differences highlight the distinctness of the two types of cavities and show that coupling occurs predominantly through fields in the air. For dielectric-mode cavities, fields within air holes in the nanobeams are weak, and evanescent fields leaking out from the edges are responsible for coupling [Fig. 2(c)]. In comparison, fields in the air holes dominate for air-mode cavities [Fig. 2(d)], and nanotubes are coupled when they are placed on top of the air holes.

Next, we compare the dielectric- and air-mode cavities by analyzing the PL spectra. We obtain the peak area and the linewidth for both the nanotube and cavity emission by performing a bi-Lorentzian fit to data [Fig. 2(g)]. We let I_{cav} and I_{CNT} be the

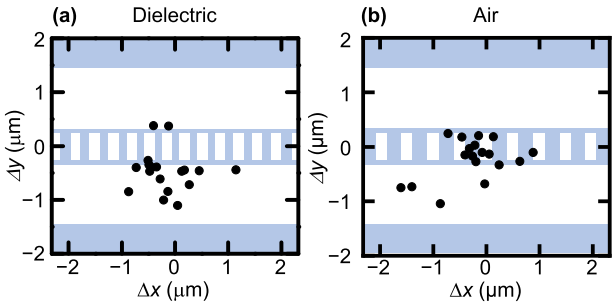

Fig. 3. (Color online) Spatial distribution of nanotubes that show coupling. (a, b) Spatial distribution of photoluminescence (PL) peak intensity locations for dielectric- and air-mode cavities. The peak locations are determined by two-dimensional Gaussian fitting, and they are plotted as a function of the displacement from the center of the cavity. The center of the cavities is taken as the origin of the coordinate system. Original data are presented in Ref. 25.

Table 1. β^* and Q_{cav} of dielectric- and air-mode cavities. Devices are measured with $P = 10\ \mu$W and λ_{ex} tuned to the E_{22} resonance. The error values are standard deviations. Original data are presented in Ref. 25.

Cavity type	Number of devices	β^*	Q_{cav}
Dielectric	16	0.18 ± 0.16	3500 ± 1400
Air	17	0.37 ± 0.30	2000 ± 700

PL peak area of the cavity and direct CNT emission, respectively, and use $\beta^* = I_{\mathrm{cav}}/(I_{\mathrm{CNT}} + I_{\mathrm{cav}})$ as a measure of the coupling efficiency. We find that the average value of β^* for the air-mode devices is more than twice that of the dielectric-mode cavities (Table 1), consistent with the expectation from the mode profiles. We also obtain the quality factor Q_{cav} of the mode from the linewidth of the cavity peak. However, the observed values are likely limited by fabrication errors as the FDTD calculations predict $Q_{\mathrm{cav}} > 10^5$.

The efficient coupling observed is reasonable because of the ultralow mode volume of the air-mode cavities. From the FDTD calculation shown in Fig. 2(d), mode volume $V = 2.37 \times 10^{-2}(\lambda_{\mathrm{cav}}/n)^3$ is obtained, where $\lambda_{\mathrm{cav}} = 1.38\ \mu$m is the cavity resonance wavelength, and $n = 1$ is the index of refraction for air. The maximum spontaneous emission enhancement factor is given by $F = (3\lambda_{\mathrm{cav}}^3 Q_{\mathrm{CNT}})/(4\pi^2 n^3 V) = 316$, where we use the quality factor of the nanotube emission $Q_{\mathrm{CNT}} = 99$ instead of Q_{cav} because the nanotube emission linewidth is much wider than the cavity linewidth.[54] Even at the top surface of the nanobeam where the nanotubes are placed, an enhancement factor of over 100 is obtained within the center air hole.

4. Spectral tuning of optical coupling to nanobeam cavities

The spectral overlap of the nanotube emission and cavity mode is an important factor in determining the quantum electrodynamical effects. This section describes the spectral tuning of air-suspended CNTs coupled to integrated nanobeam cavities.[26]

Laser heating desorbs molecules from the nanotubes, offering a simple method for adjusting the nanotube emission by reducing dielectric screening. We can modify the detuning by as much as 25 meV, inducing a drastic change in the cavity peak intensity. The cavity quantum electrodynamics model is used to analyze the data, and the spectral overlap of the nanotube emission with the cavity peak can mainly explain the enhancement of the cavity mode.

The air-mode nanobeam cavities are fabricated in a manner similar to that described in Section 3. The cavities are designed to have resonances near the emission energy of chiralities with large populations to maximize the coupling probability, and $>$ 10,000 cavities are prepared on a chip.

The devices are measured using a fully automated confocal microscope system.[15] Nanotubes optically coupled to the cavity are located using one-dimensional PL scans over the nanobeams. The automated scan results are filtered by performing peak detection and linewidth estimation. Because the cavity linewidth is considerably narrower than the nanotube linewidth at room temperature, devices showing a sharp peak component are selected for detailed characterization. The samples are placed in nitrogen to avoid nanotube oxidation at high excitation powers.

To tune the optical transition energy, we take advantage of the sensitivity of air-suspended nanotubes to dielectric screening. Large spectral shifts of up to 30 meV have been observed by controlling the amount of adsorbed molecules through temperature or pressure.[55–59] We use laser heating to induce molecular desorption in our devices, which is a simple and convenient method.

Using a device where the nanotube emission needs blueshifting by $\sim$10 meV to achieve resonance, we study the excitation power dependence of the PL spectrum [Fig. 4(a)]. As the excitation power increases, the nanotube peak blueshifts because of molecular desorption, while the cavity peak gradually brightens. The nanotube emission is brought

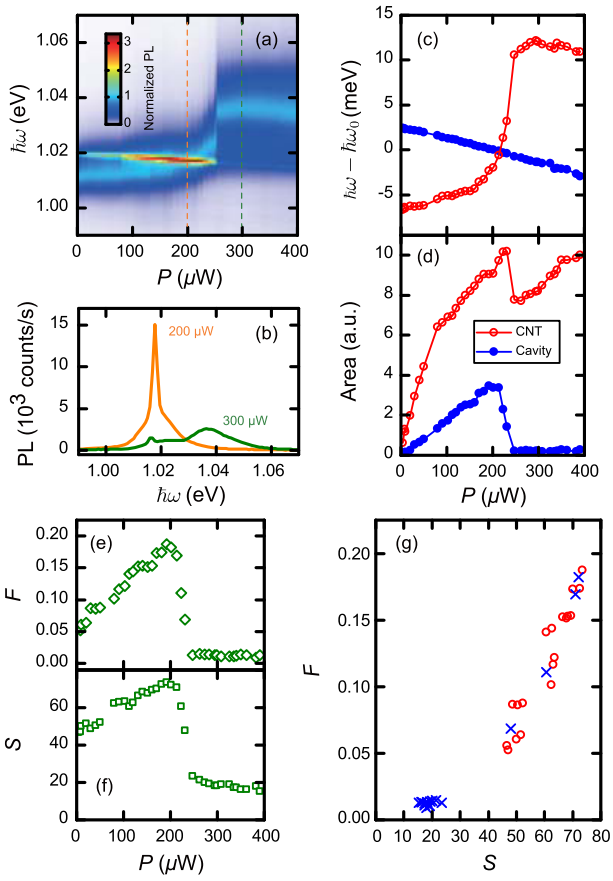

Fig. 4. (a) Excitation power dependence of photoluminescence (PL). PL is normalized with respect to the nanotube peak height. Vertical dashed lines indicate the powers where PL spectra in (b) are taken. (b) Comparison of PL spectra taken at $P = 200$ μW (orange) and 300 μW (green). (c, d) Excitation power dependence of the (c) peak center energy and (d) peak area. Red open circles are obtained from the CNT peak, and the blue dots are taken from the cavity emission. The peak center energies are plotted as the difference from the resonant energy $\hbar\omega_{cav} = 1.018$ eV. For (a–d), excitation laser energy is tuned to E_{22} resonance, and laser polarization is perpendicular to the nanobeam. (e, f) Excitation power dependence of (e) F and (f) S. (g) F as a function of S. Open circles indicate red-detuned nanotube emission conditions ($P \leq 190$ μW), and crosses correspond to blue-detuned conditions ($P > 190$ μW). Original data are presented in Ref. 26.

into resonance at $P \sim 200$ μW, enhancing cavity emission intensity. Further increasing the excitation power, the cavity peak becomes weaker again as the nanotube peak continues to blueshift. We do not find additional blueshifting above $P \sim 250$ μW because the molecules are fully desorbed.

In Fig. 4(b), we compare on- and off-resonance spectra, which are indicated by orange and green curves, respectively. We find an enhancement of the cavity peak height by a factor of 10 at resonance, whereas the nanotube peak height remains comparable. The significant difference in the cavity peak height indicates that the spectral shift modifies the optical coupling to the nanotube emission. The spectral lineshape of the nanotube peak changes at high powers (green curve), probably due to inhomogeneous molecular desorption.

The excitation power dependence is analyzed by decomposing the spectra into cavity and nanotube peak components to characterize the spectral tuning effect quantitatively. We first fit the sharp cavity peak to a single Lorentzian function using a fitting window of ~10 meV, yielding the cavity peak energy $\hbar\omega_{\rm cav}$, linewidth γ, and peak area $I_{\rm cav}$. Because of the complex nanotube lineshape, we let the nanotube peak spectrum $L_{\rm CNT}(\omega)$ be the fitting residual, where ω is the frequency. The nanotube peak area $I_{\rm CNT}$ is defined as the integral

$$I_{\rm CNT} = \int L_{\rm CNT}(\omega)\mathrm{d}\omega, \qquad [1]$$

and the peak energy $\hbar\omega_{\rm CNT}$ is defined as the weighted average

$$\hbar\omega_{\rm CNT} = \hbar\frac{\int \omega L_{\rm CNT}(\omega)\mathrm{d}\omega}{\int L_{\rm CNT}(\omega)\mathrm{d}\omega}. \qquad [2]$$

In Fig. 4(c), we plot the peak energies as a function of the excitation power, and blueshifting of the nanotube peak by as much as 18 meV (red open circles) is observed. A slight redshift of the cavity peak (blue dots) likely originates from the heating-induced refractive index increase.[60] The combined energy shifts of the nanotube and cavity allow for energy detuning $\hbar\omega_{\rm cav} - \hbar\omega_{\rm CNT}$ to be changed from +9 to −14 meV. The tuning range is sufficiently extensive for modulating the optical coupling of the nanotubes to the cavity, as it considerably exceeds the nanotube emission linewidth at room temperature. We note that the shifts are reversible upon excitation power reduction.

We now turn our attention to the excitation power dependence of emission intensities [Fig. 4(d)]. $I_{\rm CNT}$ increases linearly at low excitation powers and then becomes sublinear,[15] with a drastic drop at $P = 250$ μW [Fig. 4(d), red open circles]. Because the E_{22} resonance also blueshifts by molecular desorption,[56–59] the sudden drop can be understood by the shifting of the E_{22} resonance away from the excitation energy. In comparison, we observe a linear increase of $I_{\rm cav}$ with excitation power

for the region below $P = 190$ μW [Fig. 4(d), blue dots]. The coupling improvement likely cancels out the sublinearity of I_{CNT} because the nanotube peak approaches resonance in this power region. The cavity peak area rapidly reduces above $P = 200$ μW because of the increased energy detuning.

The power-dependent optical coupling is characterized by evaluating the emission enhancement at the cavity resonance. Assuming that stimulated emission is negligible, the spontaneous emission enhancement factor F is given by

$$F = \frac{I_{\mathrm{cav}}/C_{\mathrm{cav}}}{I_{\mathrm{CNT}}/C_{\mathrm{CNT}}}, \quad [3]$$

where C_{CNT} and C_{cav} are the collection efficiencies of the nanotube and cavity emission, respectively.

A conservative estimate of F is made by taking the largest possible value of the ratio $C_{\mathrm{cav}}/C_{\mathrm{CNT}}$. We let $C_{\mathrm{cav}} = 0.5$, supposing that the objective collects all the light emitted from the cavity mode into the upper hemisphere. For the direct nanotube emission, we use the dipole radiation pattern as if the nanotube is emitting into free space. This results in $C_{\mathrm{CNT}} = 0.25$ with the numerical aperture of 0.8 for the objective lens. We note that higher collection efficiencies are expected because of the reduced emission rate for in-plane directions caused by the photonic bandgap. As we will see in Section 5, the assumptions are too conservative, and F is significantly underestimated. Nevertheless, quantitative accuracy is not essential for the following discussion; therefore, we will proceed with this conservative estimate.

Using the data shown in Fig. 4(d), the calculated F is plotted in Fig. 4(e). As the excitation power is increased up to $P = 190$ μW, the enhancement factor increases by more than a factor of ~ 3, and F rapidly decreases by a factor of 15 at $P = 250$ μW. The extensive modification to the enhancement factor is consistent with the spectral shifts in this range. We do not observe much excitation power dependence above $P = 250$ μW.

The enhancement factor is known to be determined by the spectral overlap, spatial overlap, and polarization matching.[61),62)] Assuming that the nanotube does not move during our experiment, F should only depend on the spectral overlap. The nanotube lineshape is complex, so we must evaluate the spectral overlap without assuming a particular emitter lineshape. We first consider a simple case of a monochromatic emitter coupled to a cavity with a Lorentzian lineshape. The spontaneous emission enhancement ξ at a frequency ω is then given by

$$\xi = \frac{3}{4\pi^2}\left(\frac{\lambda_{cav}^3}{V}\right)\left(\frac{\omega}{\gamma}\right)\frac{(\gamma/2)^2}{(\omega-\omega_{\mathrm{cav}})^2+(\gamma/2)^2}, \quad [4]$$

where λ_{cav} and V are the wavelength and mode volume of the cavity, respectively.[54)] We multiply the cavity enhancement and the normalized lineshape of the nanotube emission and integrate them over the full spectrum to obtain

$$F = \frac{3}{4\pi^2}\left(\frac{\lambda_{cav}^3}{V}\right)S, \quad [5]$$

where the integral

$$S = \int\left(\frac{\omega}{\gamma}\right)\frac{(\gamma/2)^2}{(\omega-\omega_{\mathrm{cav}})^2+(\gamma/2)^2}\frac{L_{\mathrm{CNT}}(\omega)}{I_{\mathrm{CNT}}}\mathrm{d}\omega \quad [6]$$

is the generalized form of the spectral overlap. $1/S$ reduces to $1/Q_{\mathrm{cav}} + 1/Q_{\mathrm{CNT}}$ under an assumption that the nanotube lineshape is a Lorentzian resonant with the cavity,[54)] where Q_{cav} and Q_{CNT} are the quality factors of the cavity and nanotube peaks, respectively. If Q_{cav} is considerably larger than Q_{CNT}, the upper bound of S would be given by Q_{CNT}.

The spectral overlap can be calculated for arbitrary lineshapes using Eq. [6], and the numerical integration results are plotted in Fig. 4(f). When the excitation power is increased, we observe a crossover from a gradual increase to a rapid decrease at $P = 190$ μW as the nanotube peak shifts through the cavity peak. The maximum spectral overlap $S = 73$ is reasonable, considering that $Q_{\mathrm{CNT}} \sim 80$.

The correlation between the enhancement factor and the spectral overlap is examined in Fig. 4(g). Indeed, F increases monotonically with S as expected from Eq. [5]. We note the detuning changes sign above and below $P = 190$ μW, but similar enhancements are obtained for red- (open circles) and blue-detuned (crosses) nanotube emission. It is reasonable that the detuning sign does not have an effect because F should only depend on S.

Intriguingly, we observe a slight superlinearity in the F–S plot [Fig. 4(g)]. One possible explanation is the cavity-resonant optical forces. In our analysis, we assume that the spatial overlap does not change during our measurements, but it may improve at resonance if the CNTs are pulled toward the electric field maximum.[63),64)] Another possibility is stimulated emission, which contributes to additional emission into the cavity mode. In this device, the spectral overlap becomes larger at high excitation powers, which is preferable for stimulated emission.

5. Near-unity radiative quantum efficiency of bright excitons

Radiative quantum efficiency is a fundamental physical quantity that limits the efficiency of optoelectronic devices. III-V direct gap semiconductors with radiative quantum efficiencies close to 100% have played a central role in developing efficient light-emitting diodes (LEDs) that are now used ubiquitously.[65] Modern high-power diode lasers are extensively used in industries including telecommunications,[66] material processing, and medical treatments.[67] However, the performance needed for broad applications would not have been possible without the high quantum efficiencies of the gain materials. Likewise, organic semiconductors have succeeded commercially in LED displays[68] only after substantially improving their radiative quantum efficiencies.[69),70]

In this section, we experimentally determine the radiative quantum efficiencies of excitons in air-suspended CNTs.[27] Quantum electrodynamical effects in nanoscale photonic cavities are used to selectively modify the radiative decay rate of excitons, allowing us to gain insight into the fractions of radiative and nonradiative processes before the modification. Individual CNTs are coupled to air-mode photonic crystal nanobeam cavities, and PL measurements are performed to quantitatively evaluate the spectral and temporal enhancements induced by the Purcell effect. The radiative quantum efficiency of bright excitons in long air-suspended CNTs at room temperature can reach near unity.

The accelerated radiative recombination caused by the Purcell effect[53] appears in the spectral domain as an emission enhancement at the cavity mode frequency, as discussed in Sections 3 and 4. In contrast, it is more directly observed in the time domain as a shortening in the lifetime. The overall change in the decay rate can be characterized by the acceleration factor

$$A = \frac{(1+F)\gamma_{\mathrm{r}} + \gamma_{\mathrm{nr}}}{\gamma_{\mathrm{r}} + \gamma_{\mathrm{nr}}} = 1 + F\eta, \qquad [7]$$

where $\eta = \gamma_{\mathrm{r}}/(\gamma_{\mathrm{r}} + \gamma_{\mathrm{nr}})$ is the radiative quantum efficiency. If F and A are known, Eq. [7] allows us to determine η without making further assumptions. We independently evaluate the Purcell and acceleration factors by performing spectral- and time-domain measurements on excitons coupled to a microcavity.

The air-suspended tubes are coupled to silicon photonic crystal nanobeam cavities to modify the radiative decay rates by the Purcell effect,[25),26] as shown in Fig. 5(a). We use air-mode cavities characterized by ultrasmall mode volumes and large electric fields in the air holes, which allows for high-efficiency coupling, as demonstrated in Section 3.

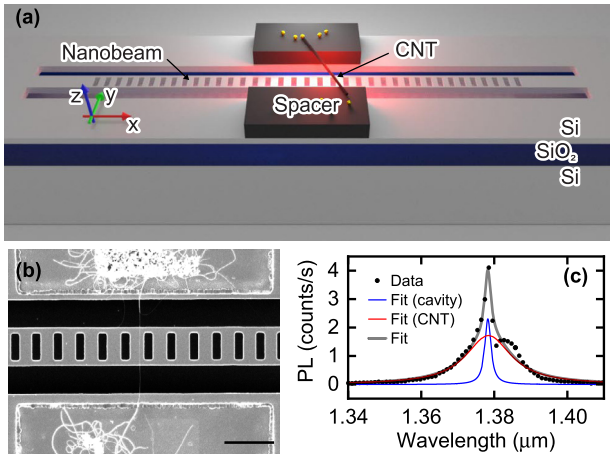

Fig. 5. (a) Schematic of the device. (b) Scanning electron micrograph of a fabricated device. A carbon nanotube (CNT) is suspended across the width of the trench near the center of the image. The scale bar is 1 μm. (c) Typical photoluminescence (PL) spectrum of a device showing optical coupling to the cavity. The dots are data, and the gray line is the bi-Lorentzian fit. The blue and red curves correspond to the cavity and CNT peak components, respectively. We interpret the asymmetry of the peak shape as a dip caused by the interference of the optics or the interference with the reflection from the bottom of the nanobeam substrate. $\lambda_{\mathrm{ex}} = 793$ nm and $P = 20$ μW are used for the excitation, and the laser polarization is parallel to the nanotube axis. Original data are presented in Ref. 27.

Because CNTs exhibit strong quenching effects upon contact with the substrate,[15),46] we place spacer layers to suspend the tubes a few hundred nanometers above the cavity. The thickness of the spacers is critical in our device design because the evanescent fields of the cavity mode decrease exponentially above the cavity. On the basis of FDTD simulation[71] results, we select a spacer layer thickness of 250 nm for which a Purcell factor of 5.8 is achievable. The nanobeams are designed to be 800 nm wide, and the hole width is fixed at 500 nm, where we have selected the parameters to compensate fabrication errors. The lattice constant a is varied from 320 to 511 nm to cover a wide wavelength range from 1100 to 1600 nm for coupling to various nanotube chiralities, and the hole length is scaled to be $0.4a$. The cavities are fabricated similarly to

the description in Section 3. A scanning electron micrograph of a device is shown in Fig. 5(b).

As the chirality and location of the nanotubes are randomly distributed, some effort is required to find tubes with good spatial and spectral overlap with the cavity modes. More than 300,000 devices are prepared to overcome the low yield of typically $< 0.1\%$ for devices with optical coupling. Automated scanning is performed to efficiently collect PL spectra from numerous devices, constructing color maps of PL intensity as a function of position and wavelength. The signature of optical coupling is the spectrally narrow peak corresponding to the cavity mode. We perform two-dimensional peak detection to extract such data, and then nonlinear curve fitting is used to determine the linewidths for each peak. We select devices for detailed characterization when the linewidth is < 5 nm, sufficiently narrower than the typical linewidths of nanotubes.

Figure 5(c) shows a PL spectrum of a representative device, where a sharp peak corresponding to the cavity mode can be observed on top of a broader peak from CNT emission into free space. The cavity peak is centered at 1378.1 nm and has a linewidth of 0.5 nm, whereas the CNT peak has a center wavelength of 1378.4 nm and a linewidth of 14.1 nm. The cavity linewidth is limited by the spectrometer resolution, and a separate measurement has been performed[27] to evaluate the actual quality factor of $\sim 2 \times 10^5$. Devices showing multiple peaks or temporal instabilities are eliminated from further measurements because they indicate bundling or contamination.[72),73)]

The PL spectrum taken at the center of the device [Fig. 5(c)] can be used to extract the Purcell factor from Eq. [3] if C_{cav} and C_{CNT} are known. To obtain the collection efficiencies, we simulate the radiation patterns by FDTD [Fig. 6(a) and (b)]. Because the cavity mode primarily consists of zone boundary waveguide modes, coupling to leaky modes above the light line is small.[44)] Most of the light that leaks out is directed at a low angle along the nanobeam [Fig. 6(a)], likely because most of the coupling occurs near the light line. As a result, only a small fraction of the cavity photons fit within the numerical aperture of the objective lens, giving $C_{\mathrm{cav}} = 0.15$. In contrast, the photonic bandgap reduces nanotube radiation at low angles, effectively redirecting the emission upward. This redirection plays a key role in the increased collection efficiency, which reaches 40% [Fig. 6(b)]. Also, considering the light collected from the length of

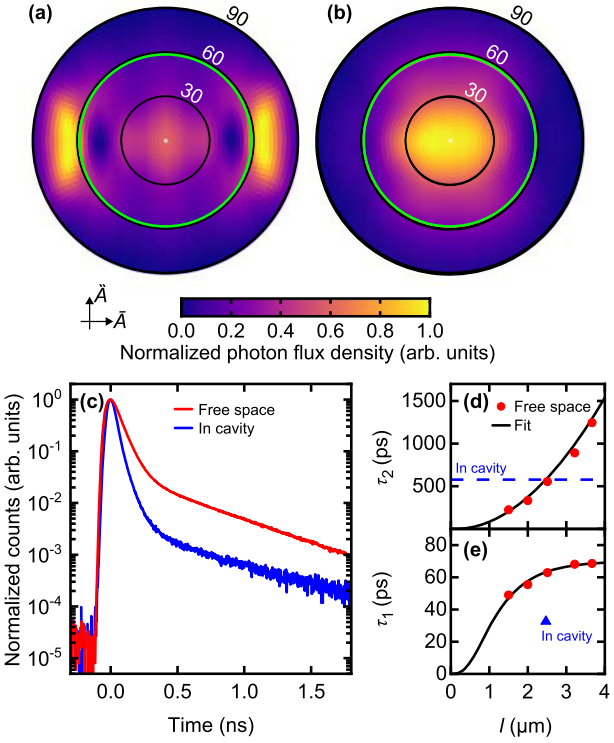

Fig. 6. (a) Calculated far-field radiation pattern of the fundamental cavity mode. (b) Calculated far-field radiation pattern of the uncoupled nanotube emission. For (a) and (b), photon flux density is plotted as a function of polar and azimuthal angles in spherical coordinates. The radial axis represents the polar angle. The green circle represents the numerical aperture of the objective lens. (c) Decay curves for (blue) the Purcell-enhanced nanotube emission from the same device as in Fig. 5(c) and (red) a 2.0-μm-long (9,8) nanotube in free space. The excitation powers are 100 and 5 nW for nanotubes in the cavity and free space, respectively. (d, e) Length dependence of (d) τ_1 and (e) τ_2 in free space. The red dots are data, and the lines are fits using the exciton diffusion model.[16)] The blue dashed line in (d) shows the dark exciton lifetime in the cavity, from which we extract the effective nanotube length. The blue triangle in (e) shows the Purcell-accelerated bright exciton lifetime. Original data are presented in Ref. 27.

the tube that extends beyond the nanobeam,[27)] we obtain $C_{\mathrm{CNT}} = 1.6$. This analysis results in the Purcell factor $F = 0.84 \pm 0.22$ for this device, which is a reasonable value.

We must evaluate the acceleration factor by performing time-resolved PL measurements, to determine the quantum efficiency. The same PL microscopy setup is used, but the devices are excited with $\sim$100 fs laser pulses, and emission is detected using a fiber-coupled superconducting single photon detector. Time-resolved PL data taken from the de-

vice shown in Fig. 5(c) are plotted as a blue curve in Fig. 6(c). We observe fast and slow decay components with lifetimes τ_1 and τ_2, respectively.[16] By comparing the decay curve with that of a nanotube in free space having a similar length [red curve in Fig. 6(c)], we can already discern a significant difference. The bright exciton lifetime, τ_1, is considerably shorter, whereas τ_2, reflecting the dark exciton dynamics, remains comparable. This result is expected because the Purcell effect accelerates the bright exciton decay, whereas the dark excitons do not interact with photons. Therefore, the cavity would not change its lifetime. We note that the contrasting behavior of bright and dark exciton lifetimes rules out extrinsic quenching effects as the cause for bright exciton lifetime shortening. Such effects, including quenching caused by contact with the substrate, should shorten both bright and dark exciton lifetimes, as in the case of end quenching.[16]

The bright exciton lifetime is extracted by fitting the data for the device with a biexponential function, and we obtain $\tau_1 = 34.8 \pm 0.3$ ps and $\tau_2 = 586 \pm 5$ ps. The change in τ_1 for the nanotube coupled to the cavity compared with a nanotube in free space is needed to obtain the value of A, but care must be taken because τ_1 is dependent on the nanotube length l.[16] We take advantage of the fact that the dark exciton dynamics is unaffected by the cavity and use the length dependence of τ_2 obtained from the exciton diffusion model[16] to determine the nanotube length at which τ_1 is compared.

Figures 6(d) and (e) show the length dependence of τ_2 and τ_1, respectively, for air-suspended (9,8) nanotubes in free space.[16] The bright and dark exciton lifetimes increase with the nanotube length due to reduced end quenching in longer nanotubes. By looking up the nanotube length for $\tau_2 = 586$ ps [Fig. 6(d), dashed line], $l = 2.5 \pm 0.1$ μm is obtained. The acceleration factor is then evaluated using the corresponding bright exciton lifetime in free space [Fig. 6(e)], and we find $A = 1.82 \pm 0.09$. The error for the acceleration factor is computed from the 1σ confidence intervals of the fits and the standard deviation of the lifetime data in free space. Having determined both F and A for this device, the radiative quantum efficiency of the bright exciton is calculated to be 0.98 ± 0.29 using Eq. [7].

Near-unity quantum efficiency is reproducibly observed in several devices. We have repeated the same measurements in additional devices with varying Purcell factors. The acceleration factor is plotted as a function of the Purcell factor in Fig. 7,

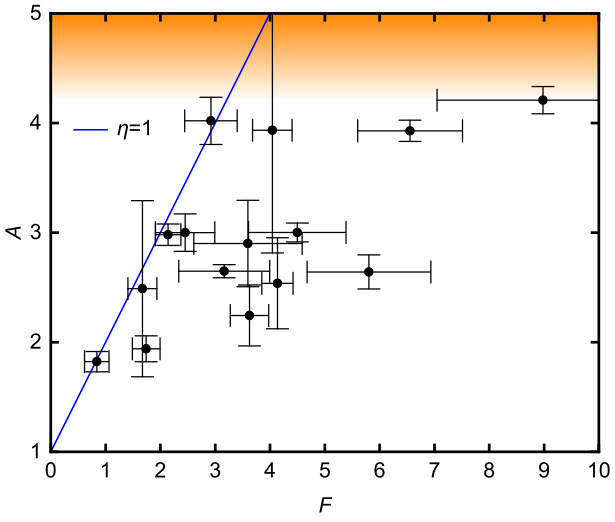

Fig. 7. (Color online) The acceleration factor as a function of the Purcell factor. The dots are data, and the error bars show the 1σ confidence interval. The line indicates $\eta = 1$ as given by Eq. [7]. Chiralities of the nanotubes in the measured devices are (9,7), (9,8), (10,8), and (11,6). Original data are presented in Ref. 27.

where variations and errors in the measured quantum efficiencies can be observed. The shaded area corresponds to the region beyond the shortest resolvable lifetimes. Data points closer to the top-left corner indicate higher quantum efficiency, and we observe that the line representing unity quantum efficiency passes through several data points within the error bars. Unsurprisingly, some devices show lower efficiencies because shorter nanotubes have higher nonradiative decay rates.[15),16] Therefore, we may interpret the highest efficiencies observed as being the intrinsic property of the bright excitons in CNTs. Even when considering the error bars of the data points, it is fair to state that their quantum efficiencies are near unity in free space.

The radiative quantum efficiency is directly related to PL yield, which is defined as the fraction of emitted photons to absorbed photons. The PL yield is not necessarily equal to the radiative quantum efficiency of the bright excitons because most of the absorbed photons end up in dark excitonic states. Because the valence and conduction bands are 4-fold degenerate, there are 16 exciton states. Only one state is bright, and all the other states are dark because of spin, momentum, and parity selection rules. The initial population of all 16 states should be equal if free carriers are generated as in the case of E_{22} excitation,[74] and a PL yield of 6.25% would

result for unity quantum efficiency of bright excitons if there are no further population redistribution. Experimentally, a similar value of ∼7% has been reported for air-suspended nanotubes at E_{22} excitation.[17] Conversion of the dark excitons to the bright excitons[16] can further increase PL yields.

Enhancing the PL yield by selecting excitation methods with a higher initial population of bright excitons should be possible. Resonant excitation can selectively populate the bright states, and in principle, unity PL yield would be achieved. If rejection of excitation laser becomes an experimental issue, an alternative is to use phonon sidebands[75] and E_{11} excited states.[56] Limiting excitation into the spin singlet manifold will improve the PL yield by a factor of 4. A more sophisticated scheme for electrical excitation, such as spin-polarized[76] or energy-selective[77] injection, will be needed.

Finally, we would like to comment on the radiative lifetime of excitons in CNTs.[78–80] When radiative quantum efficiency is unity, the bright exciton decay time is equivalent to the radiative lifetime. Therefore, we can consider the reported bright exciton decay times of air-suspended nanotubes ranging from 60 to 90 ps[16] to be their effective radiative lifetime at room temperature. In comparison, theoretical calculations[78,79] have yielded effective radiative lifetimes on the order of 10 ns at room temperature for micelle-wrapped nanotubes. However, the dielectric environment differs considerably from the air-suspended structures. The experimentally observed bright exciton decay times also show a clear family pattern,[16] which has not been addressed theoretically. Updated calculations are needed to describe radiative lifetimes in air-suspended nanotubes accurately.

6. Conclusions

This review summarizes our work on cavity coupling and quantum electrodynamics of excitons in individual air-suspended CNTs. In Section 2, silicon microdisk resonators demonstrated the feasibility of integrating telecom wavelength nanotube emitters into silicon photonics. Air-mode nanobeam cavities were introduced to achieve efficient coupling in Section 3. Molecular desorption and dielectric screening were used for spectral tuning in Section 4, where the behavior was explained in terms of the cavity quantum electrodynamics modeling. In Section 5, we determined the radiative quantum efficiency of excitons in CNT to be near unity at room temperature by performing time-resolved measurements and modeling the Purcell effect.

These results are important not only for a fundamental understanding of light-matter interaction in CNTs but also for nanoscale optical devices in the telecom band on a silicon platform. Further possibilities for scaling down monolithic photonic circuits can be envisioned, where quantum electrodynamical effects are used to achieve novel functionalities in nanoscale devices. With high-efficiency light emission and single-photon generation capabilities,[11–13] CNTs may bring breakthroughs in subwavelength silicon photonics and integrated quantum optics. For example, integrated single photon sources[14,81] could become an essential application for future room-temperature quantum technologies.

Acknowledgments

We thank S. Imamura, R. Miura, H. Machiya, R. Watahiki, T. Shimada, R. Ohta, A. Ishii, X. Liu, S. Iwamoto, Y. Arakawa, T. Uda, and D. Yamashita for their contribution to this work. Parts of this work were supported by Japan Society for the Promotion of Science (KAKENHI JP21684016, JP23104704, JP24340066, JP24654084, JP26610080,JP26870167,JP16H05962,JP16K13613, JP19J10319,JP20H02558,JP20J00817,JP20K15199, JP23H00262), Ministry of Internal Affairs and Communications (SCOPE JP102103001, JP191503001), Ministry of Education, Culture, Sports, Science and Technology (Nanotechnology Platform, Project for Developing Innovation Systems, Photon Frontier Network Program), Asahi Glass Foundation, KDDI Foundation, Canon Foundation, and RIKEN Incentive Research Project.

References

1) Thomson, D., Zilkie, A., Bowers, J. E., Komljenovic, T., Reed, G. T., Vivien, L. *et al.* (2016) Roadmap on silicon photonics. J. Opt. **18**, 073003.
2) Wang, Z., Abbasi, A., Dave, U., De Groote, A., Kumari, S., Kunert, B. *et al.* (2017) Novel light source integration approaches for silicon photonics. Laser Photon. Rev. **11**, 1700063.
3) Kong, J., Soh, H. T., Cassell, A. M., Quate, C. F. and Dai, H. (1998) Synthesis of individual single-walled carbon nanotubes on patterned silicon wafers. Nature **395**, 878–881.
4) O'Connell, M. J., Bachilo, S. M., Huffman, C. B., Moore, V. C., Strano, M. S., Haroz, E. H. *et al.* (2002) Band gap fluorescence from individual single-walled carbon nanotubes. Science **297**, 593–596.
5) Weisman, R. B. and Bachilo, S. M. (2003) Depen-

dence of optical transition energies on structure for single-walled carbon nanotubes in aqueous suspension: An empirical Kataura plot. Nano Lett. **3**, 1235–1238.
6) Gabor, N. M., Zhong, Z., Bosnick, K., Park, J. and McEuen, P. L. (2009) Extremely efficient multiple electron-hole pair generation in carbon nanotube photodiodes. Science **325**, 1367–1371.
7) Barkelid, M. and Zwiller, V. (2014) Photocurrent generation in semiconducting and metallic carbon nanotubes. Nat. Photon. **8**, 47–51.
8) McCulley, D. R., Senger, M. J., Bertoni, A., Perebeinos, V. and Minot, E. D. (2020) Extremely efficient photocurrent generation in carbon nanotube photodiodes enabled by a strong axial electric field. Nano Lett. **20**, 433–440.
9) Higashide, N., Yoshida, M., Uda, T., Ishii, A. and Kato, Y. K. (2017) Cold exciton electroluminescence from air-suspended carbon nanotube split-gate devices. Appl. Phys. Lett. **110**, 191101.
10) Graf, A., Held, M., Zakharko, Y., Tropf, L., Gather, M. C. and Zaumseil, J. (2017) Electrical pumping and tuning of exciton-polaritons in carbon nanotube microcavities. Nat. Mater. **16**, 911–917.
11) Ma, X., Hartmann, N. F., Baldwin, J. K. S., Doorn, S. K. and Htoon, H. (2015) Room-temperature single-photon generation from solitary dopants of carbon nanotubes. Nat. Nanotechnol. **10**, 671–675.
12) Ishii, A., Yoshida, M. and Kato, Y. K. (2017) Room-temperature single-photon emission from micrometer-long air-suspended carbon nanotubes. Phys. Rev. Applied **8**, 054039.
13) He, X., Htoon, H., Doorn, S. K., Pernice, W. H. P., Pyatkov, F., Krupke, R. *et al.* (2018) Carbon nanotubes as emerging quantum-light sources. Nat. Mater. **17**, 663–670.
14) Ishii, A., He, X., Hartmann, N. F., Machiya, H., Htoon, H., Doorn, S. K. *et al.* (2018) Enhanced single-photon emission from carbon-nanotube dopant states coupled to silicon microcavities. Nano Lett. **18**, 3873–3878.
15) Ishii, A., Yoshida, M. and Kato, Y. K. (2015) Exciton diffusion, end quenching, and exciton-exciton annihilation in individual air-suspended carbon nanotubes. Phys. Rev. B **91**, 125427.
16) Ishii, A., Yoshida, M. and Kato, Y. K. (2019) High efficiency dark-to-bright exciton conversion in carbon nanotubes. Phys. Rev. X **9**, 041048.
17) Lefebvre, J., Austing, D. G., Bond, J. and Finnie, P. (2006) Photoluminescence imaging of suspended single-walled carbon nanotubes. Nano Lett. **6**, 1603–1608.
18) Graf, A., Tropf, L., Zakharko, Y., Zaumseil, J. and Gather, M. C. (2016) Near-infrared exciton-polaritons in strongly coupled single-walled carbon nanotube microcavities. Nat. Commun. **7**, 13078.
19) Watahiki, R., Shimada, T., Zhao, P., Chiashi, S., Iwamoto, S., Arakawa, Y. *et al.* (2012) Enhancement of carbon nanotube photoluminescence by photonic crystal nanocavities. Appl. Phys. Lett. **101**, 141124.
20) Noury, A., Roux, X. L., Vivien, L. and Izard, N. (2015) Enhanced light emission from carbon nanotubes integrated in silicon micro-resonator. Nanotechnology **26**, 345201.
21) Pyatkov, F., Fütterling, V., Khasminskaya, S., Flavel, B. S., Hennrich, F., Kappes, M. M. *et al.* (2016) Cavity-enhanced light emission from electrically driven carbon nanotubes. Nat. Photon. **10**, 420–427.
22) Jeantet, A., Chassagneux, Y., Raynaud, C., Roussignol, P., Lauret, J. S., Besga, B. *et al.* (2016) Widely tunable single-photon source from a carbon nanotube in the Purcell regime. Phys. Rev. Lett. **116**, 247402.
23) Luo, Y., Ahmadi, E. D., Shayan, K., Ma, Y., Mistry, K. S., Zhang, C. *et al.* (2017) Purcell-enhanced quantum yield from carbon nanotube excitons coupled to plasmonic nanocavities. Nat. Commun. **8**, 1413.
24) Imamura, S., Watahiki, R., Miura, R., Shimada, T. and Kato, Y. K. (2013) Optical control of individual carbon nanotube light emitters by spectral double resonance in silicon microdisk resonators. Appl. Phys. Lett. **102**, 161102.
25) Miura, R., Imamura, S., Ohta, R., Ishii, A., Liu, X., Shimada, T. *et al.* (2014) Ultralow mode-volume photonic crystal nanobeam cavities for high-efficiency coupling to individual carbon nanotube emitters. Nat. Commun. **5**, 5580.
26) Machiya, H., Uda, T., Ishii, A. and Kato, Y. K. (2018) Spectral tuning of optical coupling between air-mode nanobeam cavities and individual carbon nanotubes. Appl. Phys. Lett. **112**, 021101.
27) Machiya, H., Yamashita, D., Ishii, A. and Kato, Y. K. (2022) Evidence for near-unity radiative quantum efficiency of bright excitons in carbon nanotubes from the Purcell effect. Phys. Rev. Res. **4**, L022011.
28) Borselli, M., Johnson, T. and Painter, O. (2005) Beyond the Rayleigh scattering limit in high-Q silicon microdisks: Theory and experiment. Opt. Express **13**, 1515–1530.
29) Soltani, M., Yegnanarayanan, S. and Adibi, A. (2007) Ultra-high Q planar silicon microdisk resonators for chip-scale silicon photonics. Opt. Express **15**, 4694–4704.
30) Michler, P., Kiraz, A., Becher, C., Schoenfeld, W. V., Petroff, P. M., Zhang, L. *et al.* (2000) A quantum dot single-photon turnstile device. Science **290**, 2282–2285.
31) Peter, E., Senellart, P., Martrou, D., Lemaître, A., Hours, J., Gérard, J. M. *et al.* (2005) Exciton-photon strong-coupling regime for a single quantum dot embedded in a microcavity. Phys. Rev. Lett. **95**, 067401.
32) Mintairov, A. M., Chu, Y., He, Y., Blokhin, S., Nadtochy, A., Maximov, M. *et al.* (2008) High-spatial-resolution near-field photoluminescence and imaging of whispering-gallery modes in

semiconductor microdisks with embedded quantum dots. Phys. Rev. B **77**, 195322.
33) McCall, S. L., Levi, A. F. J., Slusher, R. E., Pearton, S. J. and Logan, R. A. (1992) Whispering-gallery mode microdisk lasers. Appl. Phys. Lett. **60**, 289–291.
34) Xia, F., Steiner, M., Lin, Y.-M. and Avouris, P. (2008) A microcavity-controlled, current-driven, on-chip nanotube emitter at infrared wavelengths. Nat. Nanotechnol. **3**, 609–613.
35) Gaufrès, E., Izard, N., Roux, X. L., Kazaoui, S., Marris-Morini, D., Cassan, E. *et al.* (2010) Optical microcavity with semiconducting single-wall carbon nanotubes. Opt. Express **18**, 5740–5745.
36) Legrand, D., Roquelet, C., Lanty, G., Roussignol, P., Lafosse, X., Bouchoule, S. *et al.* (2013) Monolithic microcavity with carbon nanotubes as active material. Appl. Phys. Lett. **102**, 153102.
37) Fujiwara, M., Tsuya, D. and Maki, H. (2013) Electrically driven, narrow-linewidth blackbody emission from carbon nanotube microcavity devices. Appl. Phys. Lett. **103**, 143122.
38) Maruyama, S., Kojima, R., Miyauchi, Y., Chiashi, S. and Kohno, M. (2002) Low-temperature synthesis of high-purity single-walled carbon nanotubes from alcohol. Chem. Phys. Lett. **360**, 229–234.
39) Moritsubo, S., Murai, T., Shimada, T., Murakami, Y., Chiashi, S., Maruyama, S. *et al.* (2010) Exciton diffusion in air-suspended single-walled carbon nanotubes. Phys. Rev. Lett. **104**, 247402.
40) Yasukochi, S., Murai, T., Moritsubo, S., Shimada, T., Chiashi, S., Maruyama, S. *et al.* (2011) Gate-induced blueshift and quenching of photoluminescence in suspended single-walled carbon nanotubes. Phys. Rev. B **84**, 121409(R).
41) Notomi, M., Kuramochi, E. and Taniyama, H. (2008) Ultrahigh-Q nanocavity with 1D photonic gap. Opt. Express **16**, 11095–11102.
42) Eichenfield, M., Camacho, R., Chan, J., Vahala, K. J. and Painter, O. (2009) A picogram- and nanometre-scale photonic-crystal optomechanical cavity. Nature **459**, 550–555.
43) Zhang, Y., Bulu, I., Tam, W.-M., Levitt, B., Shah, J., Botto, T. *et al.* (2011) High-Q/V air-mode photonic crystal cavities at microwave frequencies. Opt. Express **19**, 9371–9377.
44) Quan, Q. and Loncar, M. (2011) Deterministic design of wavelength scale, ultra-high Q photonic crystal nanobeam cavities. Opt. Express **19**, 18529–18542.
45) Mann, D., Kato, Y. K., Kinkhabwala, A., Pop, E., Cao, J., Wang, X. *et al.* (2007) Electrically driven thermal light emission from individual single-walled carbon nanotubes. Nat. Nanotechnol. **2**, 33–38.
46) Sarpkaya, I., Zhang, Z., Walden-Newman, W., Wang, X., Hone, J., Wong, C. W. *et al.* (2013) Prolonged spontaneous emission and dephasing of localized excitons in air-bridged carbon nanotubes. Nat. Commun. **4**, 2152.
47) Gong, Y., Ellis, B., Shambat, G., Sarmiento, T., Harris, J. S. and Vučković, J. (2010) Nanobeam photonic crystal cavity quantum dot laser. Opt. Express **18**, 8781–8789.
48) Ohta, R., Ota, Y., Nomura, M., Kumagai, N., Ishida, S., Iwamoto, S. *et al.* (2011) Strong coupling between a photonic crystal nanobeam cavity and a single quantum dot. Appl. Phys. Lett. **98**, 173104.
49) Riedrich-Möller, J., Kipfstuhl, L., Hepp, C., Neu, E., Pauly, C., Mücklich, F. *et al.* (2012) One- and two-dimensional photonic crystal microcavities in single crystal diamond. Nat. Nanotechnol. **7**, 69–74.
50) Hausmann, B. J. M., Shields, B. J., Quan, Q., Chu, Y., de Leon, N. P., Evans, R. *et al.* (2013) Coupling of NV centers to photonic crystal nanobeams in diamond. Nano Lett. **13**, 5791–5796.
51) Noury, A., Roux, X. L., Vivien, L. and Izard, N. (2014) Controlling carbon nanotube photoluminescence using silicon microring resonators. Nanotechnology **25**, 215201.
52) Lefebvre, J., Homma, Y. and Finnie, P. (2003) Bright band gap photoluminescence from unprocessed single-walled carbon nanotubes. Phys. Rev. Lett. **90**, 217401.
53) Purcell, E. M. (1946) Spontaneous emission probabilities at radio frequencies. Phys. Rev. **69**, 681.
54) van Exter, M. P., Nienhuis, G. and Woerdman, J. P. (1996) Two simple expressions for the spontaneous emission factor β. Phys. Rev. A **54**, 3553–3558.
55) Finnie, P., Homma, Y. and Lefebvre, J. (2005) Band-gap shift transition in the photoluminescence of single-walled carbon nanotubes. Phys. Rev. Lett. **94**, 247401.
56) Lefebvre, J. and Finnie, P. (2008) Excited excitonic states in single-walled carbon nanotubes. Nano Lett. **8**, 1890–1895.
57) Homma, Y., Chiashi, S., Yamamoto, T., Kono, K., Matsumoto, D., Shitaba, J. *et al.* (2013) Photoluminescence measurements and molecular dynamics simulations of water adsorption on the hydrophobic surface of a carbon nanotube in water vapor. Phys. Rev. Lett. **110**, 157402.
58) Uda, T., Ishii, A. and Kato, Y. K. (2018) Single carbon nanotubes as ultrasmall all-optical memories. ACS Photonics **5**, 559.
59) Uda, T., Tanaka, S. and Kato, Y. K. (2018) Molecular screening effects on exciton-carrier interactions in suspended carbon nanotubes. Appl. Phys. Lett. **113**, 121105.
60) El Kurdi, M., Checoury, X., David, S., Ngo, T. P., Zerounian, N., Boucaud, P. *et al.* (2008) Quality factor of Si-based photonic crystal L3 nanocavities probed with an internal source. Opt. Express **16**, 8780–8791.
61) Noda, S., Fujita, M. and Asano, T. (2007) Spontaneous-emission control by photonic crystals and nanocavities. Nat. Photon. **1**, 449–458.
62) Unitt, D. C., Bennett, A. J., Atkinson, P., Ritchie, D. A. and Shields, A. J. (2005) Polarization con-

trol of quantum dot single-photon sources via a dipole-dependent Purcell effect. Phys. Rev. B **72**, 033318.
63) Ajiki, H., Iida, T., Ishikawa, T., Uryu, S. and Ishihara, H. (2009) Size- and orientation-selective optical manipulation of single-walled carbon nanotubes: A theoretical study. Phys. Rev. B **80**, 115437.
64) Mandal, S., Serey, X. and Erickson, D. (2010) Nanomanipulation using silicon photonic crystal resonators. Nano Lett. **10**, 99–104.
65) Schubert, E. F. and Kim, J. K. (2005) Solid-state light sources getting smart. Science **308**, 1274–1278.
66) Milonni, P. W. and Eberly, J. H. (2010) Laser Physics. John Wiley & Sons, New York.
67) Steen, W. M. and Mazumder, J. (2010) Laser Material Processing. Springer, London.
68) Chen, H.-W., Lee, J.-H., Lin, B.-Y., Chen, S. and Wu, S.-T. (2018) Liquid crystal display and organic light-emitting diode display: Present status and future perspectives. Light Sci. Appl. **7**, 17168–17168.
69) Adachi, C., Baldo, M. A., Thompson, M. E. and Forrest, S. R. (2001) Nearly 100% internal phosphorescence efficiency in an organic light-emitting device. J. Appl. Phys. **90**, 5048–5051.
70) Lamansky, S., Djurovich, P., Murphy, D., Abdel-Razzaq, F., Lee, H.-E., Adachi, C. *et al.* (2001) Highly phosphorescent bis-cyclometalated iridium complexes: Synthesis, photophysical characterization, and use in organic light emitting diodes. J. Am. Chem. Soc. **123**, 4304–4312.
71) Oskooi, A. F., Roundy, D., Ibanescu, M., Bermel, P., Joannopoulos, J. D. and Johnson, S. G. (2010) Meep: A flexible free-software package for electromagnetic simulations by the fdtd method. Comput. Phys. Commun. **181**, 687–702.
72) Tan, P. H., Rozhin, A. G., Hasan, T., Hu, P., Scardaci, V., Milne, W. I. *et al.* (2007) Photoluminescence spectroscopy of carbon nanotube bundles: Evidence for exciton energy transfer. Phys. Rev. Lett. **99**, 137402.
73) Matsuda, K., Kanemitsu, Y., Irie, K., Saiki, T., Someya, T., Miyauchi, S. *et al.* (2005) Photoluminescence intermittency in an individual single-walled carbon nanotube at room temperature. Appl. Phys. Lett. **86**, 123116.
74) Kumamoto, Y., Yoshida, M., Ishii, A., Yokoyama, A., Shimada, T. and Kato, Y. K. (2014) Spontaneous exciton dissociation in carbon nanotubes. Phys. Rev. Lett. **112**, 117401.
75) Torrens, O. N., Zheng, M. and Kikkawa, J. M. (2008) Energy of K-dark excitons in carbon nanotubes by optical spectroscopy. Phys. Rev. Lett. **101**, 157401.
76) Wang, J., Chepelianskii, A., Gao, F. and Greenham, N. C. (2012) Control of exciton spin statistics through spin polarization in organic optoelectronic devices. Nat. Commun. **3**, 1191.
77) Kimura, K., Miwa, K., Imada, H., Imai-Imada, M., Kawahara, S., Takeya, J. *et al.* (2019) Selective triplet exciton formation in a single molecule. Nature **570**, 210–213.
78) Perebeinos, V., Tersoff, J. and Avouris, P. (2005) Radiative lifetime of excitons in carbon nanotubes. Nano Lett. **5**, 2495–2499.
79) Spataru, C. D., Ismail-Beigi, S., Capaz, R. B. and Louie, S. G. (2005) Theory and *ab initio* calculation of radiative lifetime of excitons in semiconducting carbon nanotubes. Phys. Rev. Lett. **95**, 247402.
80) Miyauchi, Y., Hirori, H., Matsuda, K. and Kanemitsu, Y. (2009) Radiative lifetimes and coherence lengths of one-dimensional excitons in single-walled carbon nanotubes. Phys. Rev. B **80**, 081410(R).
81) Khasminskaya, S., Pyatkov, F., Słowik, K., Ferrari, S., Kahl, O., Kovalyuk, V. *et al.* (2016) Fully integrated quantum photonic circuit with an electrically driven light source. Nat. Photon. **10**, 727–732.

(Received Dec. 21, 2023; accepted Apr. 8, 2024)

Profile

Wataru Terashima was born in Tokyo in 1978. He graduated from Chiba University in 2001. Under the supervision of Professor Akihiko Yoshikawa, he received his Ph.D. in engineering from Chiba University in 2006. From 2006 to 2012, he joined the laboratory of Dr. Hideki Hirayama's group at RIKEN as a postdoctoral fellow. He has been a Permanent Research Scientist since 2012. He has conducted pioneering work on the development of unexplored quantum cascade lasers in the terahertz region using nitride semiconductors. In 2018, he transitioned to the current laboratory of Dr. Yuichiro K. Kato's group at RIKEN, continuing as a Permanent Research Scientist. His current research interests include band engineering of low-dimensional materials such as carbon nanotubes and transition metal dichalcogenides and developing optoelectronic devices based on them.

Profile

Yuichiro K. Kato was born in 1977 in Tokyo. He obtained his undergraduate degree from Keio University. In 2005, he received his Ph.D. in physics from the University of California, Santa Barbara. After conducting his postdoctoral research at Stanford University, he was appointed Associate Professor at the Institute of Engineering Innovation at the University of Tokyo in 2007. He joined RIKEN in 2016, where he is now Chief Scientist and Director of the Nanoscale Quantum Photonics Laboratory. His current research focuses on the optical properties of nanomaterials and the physics of nanoscale photonic devices, exploring novel approaches for using their quantum properties. He is a recipient of the American Association for the Advancement of Science Newcomb Cleveland Prize (2006), the Ministry of Education, Culture, Sports, Science and Technology Young Scientists' Prize (2009), and the 19th Japan Society for the Promotion of Science Prize (2022). He is a member of the Fullerenes, Nanotubes and Graphene Research Society, the Japan Society of Applied Physics, the Physical Society of Japan, the Japan Society of Vacuum and Surface Science, the American Physical Society, the American Chemical Society, Optica, and the American Association for the Advancement of Science.